

Photonic heat amplifiers based on Anderson insulators

Matteo Pioldi,^{1,*} Giorgio De Simoni,¹ Alessandro Braggio,¹ and Francesco Giazotto^{1,†}

¹*NEST, Istituto Nanoscienze-CNR and Scuola Normale Superiore, I-56127 Pisa, Italy*

A photonic heat amplifier (PHA) designed for cryogenic operations is introduced and analyzed. This device comprises two Anderson insulator reservoirs connected by lossless lines, allowing them to exchange heat through photonic modes. This configuration enables negative differential thermal conductance (NDTC), which can be harnessed to amplify thermal signals. To achieve this, we maintain one reservoir at a high temperature, serving as the source terminal of a thermal transistor. Concurrently, in the other one, we establish tunnel contacts to metallic reservoirs, which function as the gate and drain terminals. With this arrangement, it is possible to control the heat flux exchange between the source and drain by adjusting the gate temperature. We present two distinct parameter choices that yield different performances: the first emphasizes modulating the source-drain heat current, while the second focuses on the temperature modulation of the colder Anderson insulator. Lastly, we present a potential design variation in which all electronic reservoirs are thermally connected through only photonic modes, allowing interactions between distant elements. The proposal of the PHA addresses the lack of thermal transistors and amplifiers in the mK range while being compatible with the rich toolbox of circuit quantum electrodynamics. It can be adapted to various applications, including sensing and developing thermal circuits and control devices at sub-Kelvin temperatures, which are relevant to quantum technologies.

I. INTRODUCTION

The management of heat and temperature is a crucial issue in quantum technologies. Addressing this challenge opens up experimental opportunities and advances to the state of the art [1]. To achieve control over thermal properties comparable to electrical ones, it is essential to develop heat current and temperature amplifiers. The electrical transistor, vital to the success of conventional electronics, demonstrates amplifying behavior. Thus, creating a thermal equivalent operating in extremely low-temperature regimes would signify a breakthrough in heat management of the quantum nanotechnologies.

Proposals and experimental studies on heat transistors have been conducted in various contexts, including room-temperature devices [2, 3] and nanoscale phononic heat transport [4]. However, there remains a gap to be addressed for devices operating within the framework of superconducting quantum technologies [5], where a few tenths of mK are typically considered for applications such as computing [6, 7] or high-sensitivity measurements [8]. At such low temperatures, phononic degrees of freedom quickly become an ineffective heat transport medium, while quasiparticle diffusion [1, 9] and photonic radiation mechanisms start to prevail [10–19].

This article discusses a heat transistor that amplifies thermal oscillations through a combination of electronic and photonic channels, with the latter being essential, leading to the *photonic heat amplifier* (PHA) design, which, as we will see, can be also adapted to work with only photonic heat transport channels between its terminals. Using photons enables efficient heat transport in

a sub-Kelvin environment. We will examine the performance of the proposed design as a heat current or temperature modulation amplifier by utilizing negative differential thermal conductance (NDTC), as initially suggested in Ref. [20]. Even if there are other thermal amplifiers based on inelastic effects [21, 22], we think that using NDTC will make operating at extremely low temperatures possible, correspondingly providing sufficiently strong heat current control. In our proposal, NDTC occurs due to the sensitivity of the thermal transmission coefficients to the reservoirs' impedance matching [23], which may vary with temperature, as we will see. Specifically, NDTC arises from a photonic thermal contact between two Anderson insulator reservoirs, where the efficiency of heat transport τ counterintuitively increases as the temperature difference between the terminals diminishes. This behavior allows for NDTC and thermal amplification when effectively integrated into a properly designed device, as discussed later.

This paper is organized as follows: Sec. II explains how photonic NDTC is achieved; Sec. III provides a comprehensive overview of the PHA, including a discussion of the relevant regimes and the impact of the device parameters; Sec. IV details the Current Modulation Amplifier (CMA) and the Temperature Modulation Amplifier (TMA) configurations showing also a potential alternative design which is essentially a fully photonic heat transistor; finally, Sec. V concludes by summarizing the potential of the PHA and offering insights into future developments.

II. PHOTONIC NDTC

Unlike other proposals based on the interaction of reservoirs with two- and three-level systems [24], here NDTC is obtained by relying on photonic transport and

* matteo.pioldi@sns.it

† francesco.giazotto@sns.it

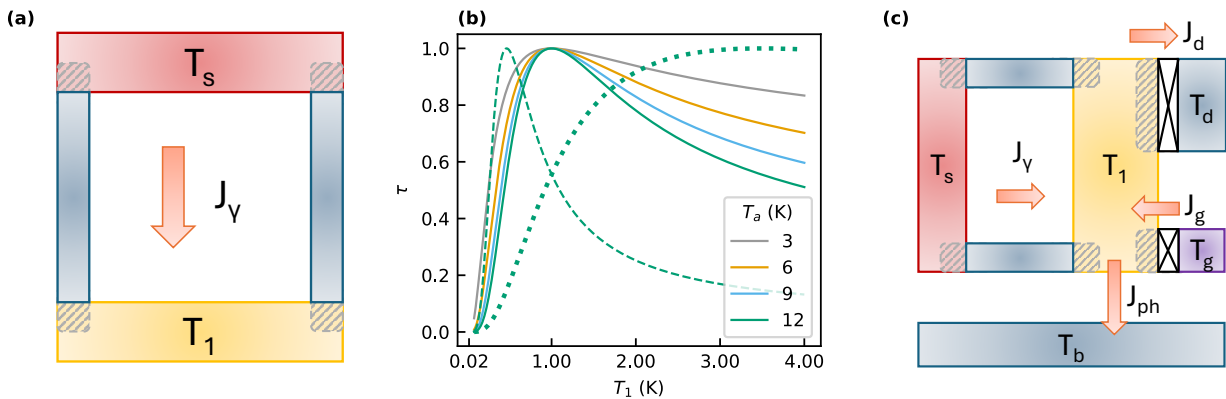


FIG. 1. **(a)** A photonic thermal link connects two Anderson insulator reservoirs. A hotter “source” reservoir at temperature T_s (shown in red) exchanges heat with a colder reservoir at temperature T_1 through photonic modes that travel across lossless waveguides (indicated in blue), contributing to a heat flux J_γ . The etched areas denote regions that are heavily doped to create low-resistance Ohmic contacts. **(b)** The thermal transmission coefficient τ , as defined in Sec. II, illustrates how efficiently heat is transmitted from one reservoir to another. The plot displays τ for different values of T_a while keeping $T_s = 1\text{K}$ constant as T_1 is adjusted. For $T_a = 12\text{K}$ both the perfectly-matched resistivity $\chi = 1$ (continuous line) and two mismatched configurations ($\chi = 5$, dashed line, and $\chi = 0.2$, dotted line) are shown, while the other curves are drawn for $\chi = 1$. **(c)** The proposed device features a central island at temperature T_1 that transfers heat currents (defined in Eqs. 2,6-7) to various terminals. The tunnel contacts to the drain and gate are positioned at heavily doped regions of the yellow central island, highlighted by the same gray etched pattern from panel (a). Each arrow indicates the positive direction of the represented heat flux. The phonon bath is maintained at temperature T_b , the gate (in purple) is at T_g , and the drain (in blue) is at T_d , always taken equal to T_b .

temperature-dependent material properties. Photonic heat transport is the main pathway for heat exchange between electronic reservoirs located below 1 K, linked by lossless superconducting lines kept well beneath the critical temperature of the superconductor [25], a typical regime for conventional dilution cryostats used in superconducting nanotechnologies. Indeed, placing two reservoirs in thermal contact via two superconducting lines, kept colder than the critical temperature, inhibits any exchange of quasiparticles, and the heat flow is mainly determined by electromagnetic fluctuations in the lines (photons) [17]. A system where heat transport occurs via photonic modes has been suggested to provide a means to achieve NDTC [26]. The impedance matching of the involved reservoirs significantly influences the heat exchange efficiency of such a mechanism.

To illustrate this concept, we adopt the simplified lumped element approximation and examine heat transport along a lossless line between two electronic reservoirs with impedances Z_s and Z_1 (see Fig. 1(a) for a diagram of such a system). In our proposal, we can neglect any capacitive and inductive components in the Anderson insulators. We assume purely dissipative and frequency-independent impedances, at least for the regime of energies more relevant to heat transport. To analyze the origin of the NDTC, we assume to keep the Anderson insulators operating at temperatures T_s and T_1 , respectively. It is crucial to mention that, generally, the electronic temperatures may influence the reservoir impedances. The lossless lines (in blue) are assumed to be thermalized at the bath temperature, and the arrow indicates the pho-

tonic heat current J_γ , which is considered positive when $T_s > T_1$ (flowing in the direction of the arrow).

The photonic heat current $J_\gamma(T_s, T_1)$ depends on the thermal transmission coefficient $\tau(T_s, T_1)$ [23] as

$$\tau(T_s, T_1) = 4 \frac{\text{Re}[Z_s(T_s)] \text{Re}[Z_1(T_1)]}{|Z_s(T_s) + Z_1(T_1)|^2}. \quad (1)$$

For two identical reservoirs, the maximum value $\tau = 1$ is achieved when $T_s = T_1$, thanks to perfect impedance matching. This is precisely illustrated in Fig. 1(b), where τ is plotted for our specific case.

Exploiting the knowledge of the expression for τ , the expression for J_γ become [23]:

$$J_\gamma(T_s, T_1) = \frac{\pi k_B^2}{12\hbar} \tau(T_s, T_1) (T_s^2 - T_1^2). \quad (2)$$

This formula lets us appreciate that if the temperature T_s is held constant and T_1 is increased from a low base value, two competing effects impact the heat current J_γ as the thermal gradient $(T_s - T_1)$ decreases. On the one hand, the reduction of the gradient should lessen J_γ ; on the other hand, the enhanced efficiency τ , resulting from better impedance matching between $Z_s(T_s)$ and $Z_1(T_1)$, tends to boost it. When the latter effect dominates, NDTC is achieved since the heat current increases even with the declining thermal gradient. The PHA will be obtained by integrating a photonic thermal channel, achieving NDTC in an aptly designed three-terminal device, like the one shown in Fig. 1(c).

A. NDTC with Anderson insulators

To achieve NDTC behavior, reservoirs with a strong temperature dependence of impedance are suitable. Anderson insulators are material systems that may meet these requirements. In fact, the resistance R_i of an Anderson insulator reservoir can be expressed as [27]:

$$R_i(T) = R_{0,i} \exp[\sqrt{T_a/T}], \quad (3)$$

where T_a is the ‘‘Anderson temperature’’ and the $i = s, 1$ subscript identifies the reservoir. $R_{0,i}$ is a constant depending on the material properties and the geometry of the reservoir. For example, this behavior is typically exhibited by neutron-transmutation doped Ge [28–30]. The transmission coefficient τ between two Anderson reservoirs with the same T_a residing at temperatures T_s and T_1 is:

$$\tau(\chi, T_a; T_s, T_1) = 4 \frac{\chi \exp[\sqrt{T_a/T_s} + \sqrt{T_a/T_1}]}{(\chi \exp[\sqrt{T_a/T_s}] + \exp[\sqrt{T_a/T_1}])^2}, \quad (4)$$

where the ratio $\chi = R_{0,s}/R_{0,1}$ describes geometrical or material differences, and it can be even redefined to include the case of different values of T_a between the two reservoirs.

This expression assumes that the contacts between the lossless lines and the reservoirs can be neglected with respect to the intrinsic Anderson insulator resistances. Indeed, a low-resistance contact to an Anderson insulator can be achieved by heavily doping the region corresponding to the contact itself, making the material locally metallic. This technique is commonly used in semiconductor materials to create Ohmic contacts [28]. Heavily doped metallic regions in our images will present an etched pattern, as shown in Fig. 1(a) near the contacts with the superconductor. We assume that the electrons in these heavily doped regions thermalize with the other electrons in the Anderson insulator reservoirs on a timescale much shorter than the operating timescales of the device.

The dependence of τ on T_1 is plotted in Fig. 1(b) for different values of the Anderson temperature, T_a , while T_s is kept fixed at 1 K. In the plot, the range of T_1 extends from 20 mK, *i.e.*, a base temperature routinely achievable in a dilution fridge, to 4 K.

We can observe that, for values of T_1 close to the base, τ tends to 0. This is because $Z_s(T_s = 1 \text{ K})$ and $Z_1(T_1)$ are heavily mismatched, suppressing the heat flow. Instead, for $T_1 = T_s = 1 \text{ K}$, when $\chi = 1$, the nominal maximum value $\tau = 1$ is achieved, thanks to the perfect matching of the two impedances. In this case, if the value of T_1 is higher than T_s , the increasing difference between Z_s and Z_1 lowers the value of τ , explaining the peaked dependence of τ on T_1 in the figure. Also two configurations of mismatched resistivity, $\chi = 5$ (dashed line) and $\chi = 0.2$ (dotted line) are considered for $T_a = 12 \text{ K}$. We need to remember that an Anderson insulator’s resistivity decreases with temperature. Consequently, when $\chi = 5$, the perfect matching is achieved for $T_1 < T_s$, while for $\chi = 0.2$, we need higher values of T_1 , resulting in the slope of τ being less steep.

Fig. 2 demonstrates that the source-island channel in the device achieves NDTC. The photonic heat current J_γ follows Eq. 2 and is plotted in Fig. 2(a,c) as a function of T_1 , for different values of T_a , (keeping $T_s = 1 \text{ K}$ like in Fig. 1b). For each horizontal cut, NDTC is achieved for the values of T_1 to the left of the maximum: in these intervals, raising the temperature of the colder reservoir increases J_γ .

We can also appreciate how the position and height of the maximum depend on T_a from Fig. 2(c), where the horizontal cuts correspond to the plots of Fig. 2(a) with $\chi = 1$. From this figure, we see that for higher values of T_a , this maximum gets smaller and shifts towards higher values of T_1 . This is because, for lower values of T_a , the transmission coefficient τ rises faster with T_1 (see Fig. 1(b)). The two mismatched configurations plotted for $T_a = 12 \text{ K}$ show how, for $\chi > 1$, the maximum is achieved for lower temperatures of the cold reservoir, and the opposite holds for $\chi < 1$, with consequences on the extension of the NDTC temperature range. Also, the maximum height is affected: the smaller χ , the better the matching when T_1 is low, and the temperature gradient is high, so there is a greater total heat flux.

After demonstrating the temperature dependence of the heat current, we can examine the differential thermal conductance of the photonic channel. It is defined as the derivative with respect to T_1 (with negative sign) of J_γ (see Ref. [20]):

$$\kappa_\gamma = -\frac{\partial J_\gamma}{\partial T_1} = \frac{\pi k_B^2}{12\hbar} \tau \left[2T_1 + \sqrt{\frac{T_a}{T_1^3}} \left(\frac{1}{2} - \frac{\exp[\sqrt{T_a/T_1}]}{\chi \exp[\sqrt{T_a/T_s}] + \exp[\sqrt{T_a/T_1}]} \right) (T_s^2 - T_1^2) \right]. \quad (5)$$

Indeed, κ_γ achieves negative values, as it can be seen in Fig. 2(b), where it is plotted for $T_s = 1 \text{ K}$ while varying T_1 . These negative values correspond to the NDTC range of T_1 described in Fig. 2(a,c). The term with the nega-

tive sign inside the square brackets could make the full expression negative. This term comes from the derivative of τ , so the steeper τ , the more negative κ_γ can get. Consequently, in the mismatched cases, κ_γ dips at nega-

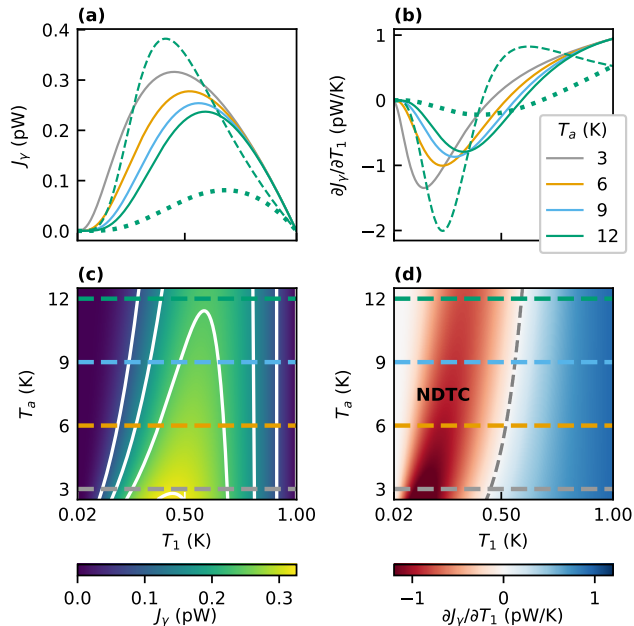


FIG. 2. In all the plots of this figure, quantities are evaluated for $T_s = 1$ K. **(a-b)** The dependence of the photonic heat current J_γ (see Eq. 2) and the differential thermal conductance κ_γ (see Eq. 5) on T_1 for different values of T_a . For $T_a = 12$ K both the perfectly matched $\chi = 1$ (continuous line) and two mismatched configurations ($\chi = 5$, dashed line, and $\chi = 0.2$, dotted line) are shown. **(c)** A color map of the intensity of the heat current between the reservoirs as a function of the temperature T_1 and the Anderson temperature T_a , where the cuts correspond, with the same color scheme, to the curves plotted in panel (a) for $\chi = 1$. **(d)** A color map of the differential conductance κ_γ as defined in Eq. 5, as a function of T_1 and T_a , with the dashed gray line delimiting the NDTC region (where $\kappa_\gamma < 0$, in red); the cuts correspond, with the same color scheme, to the curves plotted in panel (b) for $\chi = 1$.

tive values deeper and more rapidly in T_1 for $\chi > 1$ and the opposite for $\chi < 1$.

A more comprehensive view of the dependence of κ_γ on T_1 and T_a is given in Fig. 2(d). The figure represents in red the region of the T_1 - T_a plane (delimited by the gray dashed line) for which the photon heat transport channel exhibits NDTC. This region is somewhat extended for every value of T_a , assuring that the effect is robust concerning the properties of the Anderson insulator. The position and value of the minimum of κ_γ depend on the value of T_a . In particular, we notice that the NDTC effect is more intense for lower values of T_a .

Having acknowledged the effects of $\chi \neq 1$ on the range and value of NDTC, we will always assume it to be equal to 1 in the following.

III. DEVICE AND TEMPERATURE CONTROL

A. Thermal transistor

We integrate the structure described in Sec. II in a three-terminal device, like the one of Fig. 1(c), to obtain a thermal amplifier following the blueprint of Refs. [20] and [31]. We propose a device where the “S” reservoir plays the role of the source terminal and “1” is the central island, connected to the other two terminals, respectively, a gate “G” and a drain “D”. The drain and the gate are metallic reservoirs with tunnel coupling to the central island, with tunnel resistances R_d and R_g and temperatures T_d and T_g . We will assume that the drain reservoir is well thermalized to the substrate phonon bath (thanks to a strong electron-phonon coupling or large volumes of the terminals), so we will always take $T_d = T_b$. We will consider, along with the photonic heat flow J_γ , the other heat currents associated with the central part of the device: the input gate flow J_g from the gate, the output drain current J_d at the drain at temperature T_d , and the heat J_{ph} dissipated to the phonon bath. The arrows indicate the directions in which the respective currents are considered positive.

We assume that the regions of the Anderson insulator corresponding to the tunnel contacts are metallic thanks to heavy local doping, like the contacts of Sec. II, so that we can describe the energy exchange with the gate and the drain with the equations for heat transport across a NIN junction where the tunnel electrical resistance is temperature independent [32]. In this case, the expression for such tunnel heat current J_i ($i = g, d$) between a hot terminal at temperature T_{hot} and a cold one at T_{cold} is:

$$J_i(R_t; T_{hot}, T_{cold}) = \frac{\pi^2 k_B^2}{6e^2 R_i} (T_{hot}^2 - T_{cold}^2), \quad (6)$$

which is determined by the quasiparticle tunneling between two Fermi liquids kept at different temperatures, *i.e.*, a NIN tunnel junction with electrical resistance R_i ¹.

To complete our description, we consider the heat lost to the phonon bath. J_{ph} depends on the temperatures T_1 and T_b in this way (supposing vanishing Kapitza resistance for the central island):

$$J_{ph}(\Sigma, V; T_1, T_b) = \Sigma V (T_1^6 - T_b^6), \quad (7)$$

which is a model in line with Ref. [28, 33], where Σ is a parameter that describes the intensity of the electron-phonon thermal coupling, and V is the volume of the central island, with $\Sigma \approx 1 \times 10^7$ Wm⁻³K⁻⁶.

¹ In those formulae, we are simply assuming that Wiedemann-Franz laws apply to the junction. However, our model requires only that heat conductance is linear with the temperature gradient, *i.e.*, Fourier laws.

Device	T_a (K)	T_s (K)	R_g (k Ω)	R_d (k Ω)	V (m ³)	T_b (K)
CMA	12	1.4	10	10	5×10^{-18}	0.02
TMA	12	1.3	20	10	5×10^{-19}	0.02

TABLE I. The choices of parameters for the Current Modulation Amplifier (CMA) and the Temperature Modulation Amplifier (TMA). T_a is the Anderson temperature of the reservoirs; T_s is the source temperature; R_g and R_d the tunnel resistances to the gate and the drain terminals, respectively; V the volume of the central island and T_b the phonon bath temperature.

In the PHA, the temperature of the central island, and consequently the heat transport properties, is determined by the balance of the incoming and outgoing heat currents, whose expressions are reported in Eqs. 2, 6-7. Once T_s , T_g , and $T_d = T_b$ are fixed, the equation:

$$J_\gamma(T_a; T_s, T_1) + J_t(R_g; T_g, T_1) - J_t(R_d; T_1, T_d) - J_{ph}(\Sigma, V; T_1, T_b) = 0, \quad (8)$$

once solved numerically, determines the solution T_1 .

B. Parameters and temperature control

We will focus on two possible parameter configurations, shown in Tab. I. These configurations are optimized to amplify gate current modulations (CMA) or gate temperature modulations (TMA). The choice of parameters was conducted to show a configuration offering both raw performance and extended operating range while free from hysteresis effects.

To show the influence of the parameters on the performances, the solutions of Eq. 8 in the T_g - T_1 plane are plotted in Fig. 3(a-e) for various configurations. In particular, in each panel, one or more device parameters are varied while the others are taken from the first line of Tab. I. For now, we will not change $T_b = T_d$, so to describe the performance of the device in a fixed range of gate temperatures (from 20 mK to 1.4 K). However, we will see that the amplifying behavior is relatively robust with respect to the bath temperature in Secs. IV A-IV B.

In Fig. 3a, we show the behavior of T_1 as a function of T_g for different choices of the Anderson temperature. We can see that for $T_a = 3$ K and 6 K there are multiple possible values of T_1 for a single value of T_g . In this case, the PHA will present hysteresis on T_1 . We will avoid such a regime to obtain history-independent properties: this is the reason behind the choice of $T_a = 12$ K for the proposed devices. However, this hysteretic behavior may be used to define a thermal memory (a possibility that we will discuss in the following research and not hereafter).

In Fig. 3a, we also show how changing T_a affects the steepness and position of the inflection point in $T_1(T_g)$, which is pivotal to the operation range of the device and its performances. In fact, around such a point, T_1 is most

responsive to variations in the temperature or current of the gate and influences the behavior of the whole device, achieving amplification. This steepness is also affected by T_s (Fig. 3(b)), the values of the tunnel resistances R_g and R_d (Fig. 3(c)) and their ratio R_d/R_g (Fig. 3(d)).

The source temperature T_s is the only parameter that can be varied while using the device at fixed bath and drain temperatures. As shown in Fig. 3(b), it acts on both the inflection point's position and the temperature dependence's steepness. So, regulating T_s is a way to tune the PHA. This is similar to an electrical transistor, where the performance is partially tuned by changing the bias at the source terminal.

The values of tunnel resistances are also relevant. In particular, it is possible to see (Fig. 3(c)) that greater values of R_d and R_g , reducing the thermal contact of the island to the gate and the drain, favor a steep increase of T_1 as soon as τ becomes high enough. In comparison, lower values of the tunnel resistances smoothen such behavior. As seen in Fig. 3(d), the ratio between the resistances also plays a role since the lower R_d , the better the coupling to the drain (which is the coldest terminal): thus, T_1 gets lower (when the ratio R_d/R_g is varied, it is done by keeping the resistance of their parallel constant and equal to 5 k Ω).

Lastly, in Fig. 3(e), the role of the central island volume V , which determines the coupling strength to the phonon bath (Eq. 7), is highlighted. In particular, the smaller it is, the less coupled to phonons the central island becomes, resulting in the observation of a more significant excursion of T_1 .

C. Amplifier bandwidth

We need to estimate the relaxation time, τ_{rel} , for the temperature of the electrons in the central island to assess the amplifier bandwidth. This indicates the time required for the electronic temperature to achieve stationary equilibrium and respond to temperature variations at the terminals. An approximate linear estimation of this time can be given by [34]:

$$\tau_{rel} = \frac{C_1}{\kappa_{tot}}, \quad (9)$$

where C_1 is the thermal capacitance of the electron of the central island, which is the product between the island volume V and its specific heat $c_1 = \gamma T_1$, $\gamma = 1 \text{ Jm}^{-3}\text{K}^{-2}$ [35] and κ_{tot} is the total thermal conductance between the electronic degrees of freedom of the involved reservoirs.

A first conservative estimate for τ_{rel} can be given by accounting only for the contribution of phonon heat channel, approximating $\kappa_{tot} \approx \kappa_{ph} = \partial J_{ph} / \partial T_1$. So we get $\tau_{rel,ph} = \gamma / 6 \Sigma T_1^4$, which is volume independent (κ_{ph} is evaluated in Appendix A). By taking $T_1 = 20$ mK, we get the maximum $\tau_{ph} \approx 100$ ms. Knowing that phonon heat transport is relatively inefficient at low temperatures, a

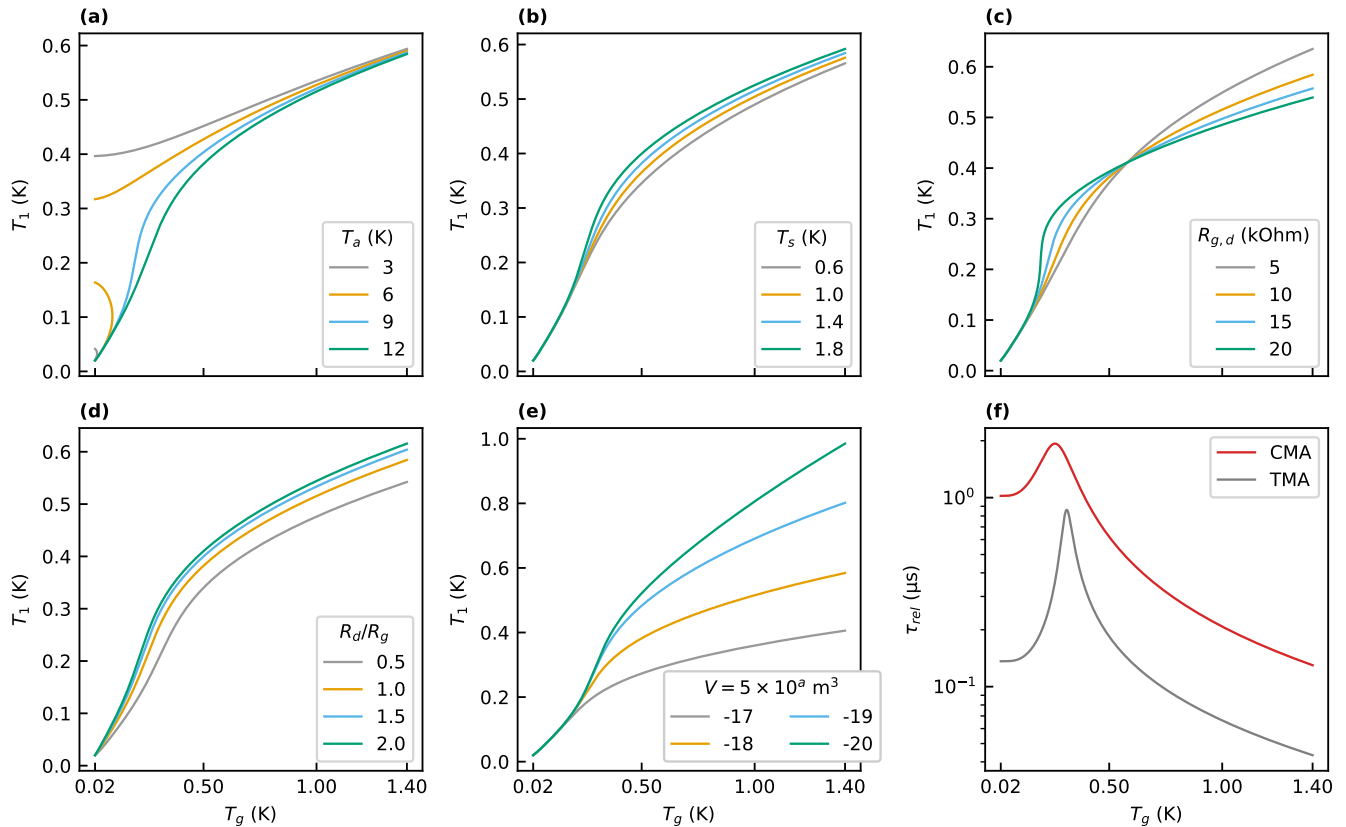


FIG. 3. (a)-(e) The sets of points in the T_1, T_g plane for which the balance of Eq. 8 is satisfied for different choices of the device parameters (one per image, reported in the legend), with the others kept as reported in the first line of Tab. I; in (d) the ratio of the resistances is varied while keeping the resistance of their parallel constant and equal to $5 \text{ k}\Omega$. (f) The dependence of the relaxation time conservative estimate τ_{rel} on the gate temperature T_g , for the CMA (red) and the TMA (gray), in logarithmic scale.

more precise evaluation can be given by estimating κ_{tot} as the sum of the conductances presented in Eq. 5 and Appendix A. The temperature dependence of κ_{tot} determines a non-monotonic behavior of the relaxation time τ_{rel} with the temperature, being

$$\tau_{rel} = \frac{\gamma V T_1}{\kappa_{tot}(T_1)}, \quad (10)$$

which is shown in Fig. 3(f), where we plotted τ_{rel} for the two different device proposals. This non-monotonic behavior directly reflects that κ_γ , starting from low temperatures, arrives at a minimum negative value as presented in Fig. 2. Instead all the other thermal conductances κ_d , κ_g and κ_{ph} , respectively toward the drain, the gate and the phonon baths, increase with T_1 . When $\kappa_\gamma < 0$, a positive temperature fluctuation $\Delta T_1 > 0$ increases J_γ . The increasing heat flux from the source partially compensates the rebalancing losses, slowing down the relaxation.

The relaxation time determines the devices' bandwidth since $\Delta f \approx 1/\tau_{rel}$. Even in the worst case, the result is of the order of the MHz, putting the PHA on par with molecular thermal switches already described in litera-

ture [36], while it also offers the functionalities of an amplifier.

IV. THERMAL AMPLIFIERS

Thanks to the knowledge gained by exploring the space of parameters of the previous section, it is possible to propose devices that achieve the best performance. In the following, we will first study the CMA device in Sec. IV A. After that, by exploiting the fact that a slight change in T_g can strongly alter T_1 , we propose the TMA device in Sec. IV B. Lastly, we show an alternative, fully photonic setup in Sec. IV C.

A. Current Modulation Amplifier (CMA)

The CMA, thanks to an apt choice of parameters (see Tab. I for its specifications), responds to a small oscillation on the gate thermal current J_g , inducing a variation on J_γ and J_d , possibly with an amplification ratio. So,

we can introduce the amplification factors ($i = \gamma, d$)

$$\alpha_i = \left| \frac{\partial J_i}{\partial J_g} \right|, \quad (11)$$

which can be computed in a linear approximation as [31], using the heat current conservation $J_g = J_d - J_\gamma + J_{ph}$:

$$\alpha_i = \left| \frac{\partial J_i}{\partial T_1} \frac{\partial T_1}{\partial (J_d - J_\gamma + J_{ph})} \right| = \left| \frac{\kappa_i}{\kappa_d + \kappa_\gamma + \kappa_{ph}} \right|, \quad (12)$$

where the conductances are taken from Eq. 5 and Appendix A.

Eq. 12 clarifies why the NDTC regime allows to obtain a heat current amplifier $\alpha_i > 1$. This requires that the numerators are more significant than the denominators. However, as long as κ_γ and κ_d are both positive, it will not be the case, but if $\kappa_\gamma < 0$, this becomes possible [20].

With our specific choice of parameters, it is possible to achieve amplification factors as great as 15 on both the source and drain, as seen in Fig. 4(a). The maximum gain value is achieved at $T_g = 260$ mK.

In analogy with Ref. [37], to evaluate the device performance, we introduce the figure of merit of the ‘‘Input Active Range’’ IAR_{CMA} . This is the range of values of J_g for which the amplification factor at the drain is greater than 1. The IAR_{CMA} goes from 0 to the black dashed line in Fig. 4(b). At $T_b = 20$ mK, $IAR_{CMA} = 50$ fW. This interval is mainly limited due to the high gain that saturates to the maximum available heat current from the source.

We can also evaluate the ‘‘Output Active Range’’ OAR_{CMA} as the range of the possible J_d values that the PHA can feed as an output while in the amplifying regime. At $T_b = 20$ mK, $OAR_{CMA} = 130$ fW. This range of values of the drain currents goes from 0 to the gray dashed line in Fig. 4(b). We also notice that, while we defined and evaluated these figures of merit referring to the drain current, the gate input shows a similar degree of control also on the source current, apart from being less effective for low values of J_g and T_g .

It is, in principle, possible, by properly changing the CMA’s parameters, to obtain higher amplification factors, arriving even at diverging values in Eq. 12. Indeed, higher gains are obtained when a greater responsivity of T_1 to variations of T_g is achieved: that is to say, for the choices of parameters that make the curves of Fig. 3(a-e) steeper. However, there is a price to pay since diverging gains correspond to strong distortion of the amplifier’s linearity. So, we choose to show a typical configuration where the gain is still substantial but less signal distortion is introduced. Those parameters also achieve better values of the input range and avoid saturation.

In Fig. 4(b), the values of the currents at play are represented. In particular, it is possible to see that, in the amplifying regime, a smaller gate current J_g drives greater fluxes. It is also interesting to estimate the switching ratio η [38] between the ‘‘OFF’’ and ‘‘ON’’ state

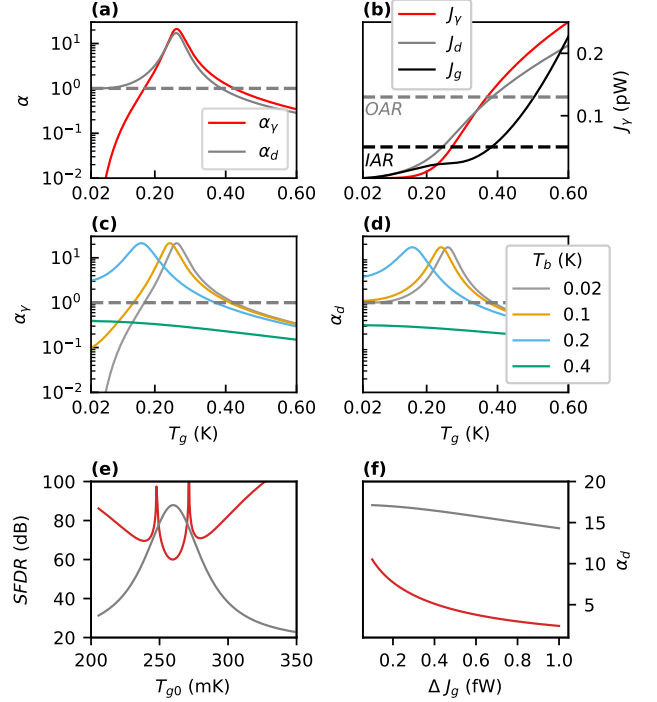


FIG. 4. The plots of this image represent the behavior of the CMA with the parameters of the first line of Tab. I; (a) The amplification factors α_γ and α_d as a function of T_g for a bath temperature $T_b = 20$ mK in logarithmic scale, with the gray dashed line $\alpha = 1$ that highlights the region where the amplification factors are greater than 1. (b) The values of J_γ , J_d and J_g , in the same configuration of panel (a), with the maximum gate current of the IAR_{CMA} and the maximum drain current of the OAR_{CMA} indicated respectively by the black and the gray dashed lines. (c)-(d) α_s and α_d at various bath temperatures T_b . (e) The $SFDR$ (red) and the gain α_d (gray) for an input heat current J_g modulation of amplitude 0.1 fW as a function of the working point T_{g0} at $T_b = 20$ mK. (f) The $SFDR$ (red) and the gain α_d (gray) at the point of maximum gain $T_{g0} = 260$ mK as a function of the amplitude ΔJ_g of the input current J_g modulation at $T_b = 20$ mK.

of the PHA ($i = \gamma, d$)

$$\eta_i = \frac{J_i^{\text{ON}}}{J_i^{\text{OFF}}}. \quad (13)$$

To evaluate such figure of merit in a configuration where J_g is lower than $J_{\gamma,d}$, we propose $T_g = T_b = 20$ mK as the OFF state and $T_g = 400$ mK (the upper limit of the amplification regime) as the ON state. For both the source and the drain currents, $\eta_i > 1000$, on par with other thermal switching factors experimentally recorded for room temperature devices [36].

In Fig. 4(c-d), $\alpha_\gamma(T_g)$ and $\alpha_d(T_g)$ are plotted, always with the parameters of Tab. I, except for T_b , which is varied to show the resilience of PHA amplifier to the background temperature setting. In particular, it is possible to see that the amplifying behavior near the maximum

is practically unmodified up to $T_b = 100$ mK. Even at $T_b = 200$ mK, the theoretical maximum value of the amplification factors is close to 15, but it would require an unusual configuration with the gate cooler than the bath.

In the PHA, amplification of an input modulation may happen with distortion. To estimate it, we evaluate the ‘‘Spurious-Free Dynamic Range’’, which is related to the ratio between the first harmonic A_1 and the second largest harmonic A_M of the device’s response J_d to a small sinusoidal modulation of the input J_g . According to the formula of Ref. [39]:

$$SFDR = 20 \log_{10} \left(\frac{A_1}{A_M} \right), \quad (14)$$

which is expressed in dB. Further details on the estimate of this figure of merit are given in Appendix B. In Fig. 4(e-f) the $SFDR$ (in red) is plotted, together with the drain gain α_d (in gray), as a function of the working point T_{g0} , for a small modulation of the input current of amplitude 0.1 fW (Fig. 4(e)) and as a function of the modulation of the amplitude ΔJ_g at the point of maximum gain $T_{g0} = 260$ mK (Fig. 4(f)). We observe that the point of maximum gain corresponds with the greatest anharmonicity and that the linearity of the response decreases with the modulation amplitude. However, we notice that the $SFDR > 20$ dB and $\alpha_d > 15$ up to $\Delta J_g = 1$ fW, which corresponds to a modulation of the 4% on the total input current $J_{g0}(T_{g0} = 260 \text{ mK}) \approx 25$ fW.

With the modalities presented in Appendix C, we also estimate the CMA’s Noise Equivalent Power (NEP). In particular, in this case, for the working point $T_g = 260$ mK the input NEP is $\text{NEP}_{CMA} = 1.0 \times 10^{-7} \text{ pW}/\sqrt{\text{Hz}}$.

It is worth noticing that the amplifying behavior is not dependent on the fact that the source and the central island are in the Anderson localization regime and that it can also be obtained for a Mott insulator (where the fraction $1/T$ at the exponent is raised to a power of $1/4$ [40]), with the drawbacks of less control on the amplification factors and less extended input ranges.

B. Temperature Modulation Amplifier (TMA)

In this specific configuration, a slight variation of T_g can induce a more remarkable change in T_1 . In particular, in this section, we present how the TMA device (with the parameters of Tab. I) achieves this.

In such a device, the fundamental figure of merit is the differential gain \mathcal{G} that, in the linear approximation, is the ratio between the output T_1 , and the input T_g oscillation amplitudes, *i.e.*

$$\mathcal{G} = \frac{\partial T_1}{\partial T_g}. \quad (15)$$

keeping fixed all the other temperatures (T_s, T_d, T_b). For the device we are considering, $T_1(T_g)$ (Fig. 5(a)) and

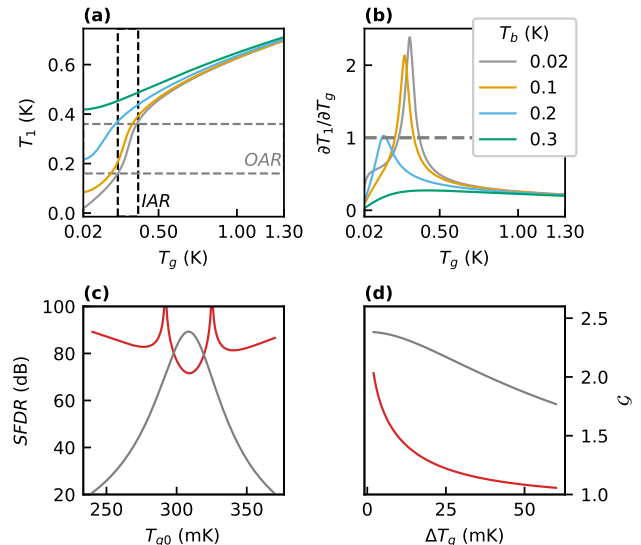


FIG. 5. The plots of this image represent the behavior of a device with the parameters of the second line of Tab. I; (a) The dependence of T_1 on T_g , for various bath temperatures T_b , with the T_g range of the IAR_{TMA} at $T_b = 20$ mK delimited by black dashed lines and the corresponding T_1 s of the OAR_{TMA} by gray dashed lines. (b) the differential gain $\partial T_1/\partial T_g$ as a function of T_g , with a gray dashed line dividing the region of actual gain where $\partial T_1/\partial T_g > 1$ from the region of lower gain, also in this case plotted for different values of T_b . (c) The $SFDR$ (red) and the gain \mathcal{G} (gray) for an input modulation of T_g of amplitude 2 mK as a function of the working point T_{g0} at $T_b = 20$ mK. (d) The $SFDR$ (red) and the gain \mathcal{G} (gray) at the point of maximum gain $T_{g0} = 310$ mK as a function of the amplitude ΔT_g of the input temperature modulation on T_g at $T_b = 20$ mK.

the corresponding $\partial T_1/\partial T_g$ (Fig. 5(b)) are shown for a selection of bath temperatures T_b . Up to $T_b = 100$ mK the amplitude of the output oscillations can be more than double the input ones, with a maximum value $\mathcal{G}(T_g = 310 \text{ mK}) = 2.5$ achieved for the coldest bath.

We can define the IAR_{TMA} and the OAR_{TMA} in this case, in analogy with what is done in Sec. IV A, with the difference that they are expressed in temperature ranges. At $T_b = T_d = 20$ mK the $IAR_{TMA} = 130$ mK (calculated as the width of the interval of T_g s for which $\mathcal{G} > 1$, delimited by black dashed lines in Fig. 5(a)), higher with respect to other examples of temperature amplifiers [37], where the IAR is of the order of tens of mK. Referring to the T_1 outputs corresponding to this input range, $OAR_{TMA} = 200$ mK, as can be measured from the data of Fig. 5(a), where they are delimited by gray dashed lines.

In Fig. 5(c-d), the $SFDR$ is plotted alongside an estimate of \mathcal{G} , given as the ratio between the first harmonic of the output A_1 and the amplitude ΔT_g of the input. In this case, as explained in Appendix B, we analyze the response regarding the central island temperature T_1 to a sinusoidal modulation of T_g at a specific working point.

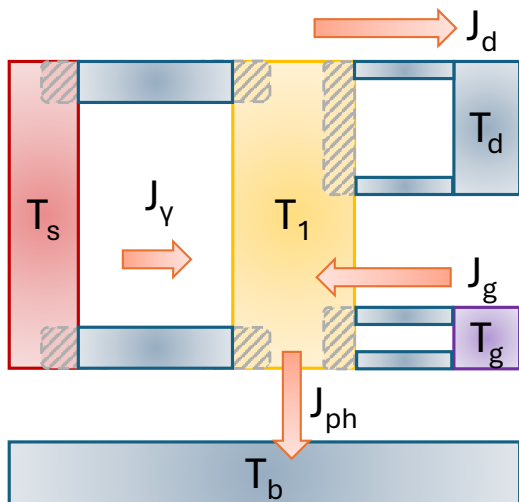


FIG. 6. A possible variation on the design of Fig. 1 features tunnel barriers replaced by lossless lines that are thermalized to the phonon bath, closing the loop on an Ohmic region of the Anderson insulator. This design enhances the flexibility of photonic heat transport and its long-range connectivity to the drain and gate channels.

These quantities are plotted in two ways: as a function of the average gate temperature T_{g0} and the modulation amplitude ΔT_g . When the modulation amplitude is considered, we took $T_{g0} = 310$ mK, which is the point of maximum gain and correspondingly should also be the point of greatest anharmonicity, as anticipated in Fig. 5(c). In particular, it is interesting to see that even for modulations of tens of mK, the anharmonicity is kept under control, with more than 20 dB between the carrier and the second greatest harmonic. At the same time, the gain remains around a value of 2.

Also, in this case, as shown in Appendix C, it is possible to estimate the total noise spectral density on the central island and infer the NEP on the input at the gate. In particular, dividing by the thermal conductance, we can assume the noise equivalent temperature oscillation $NET_{TMA} \approx 5.6 \mu\text{K}/\sqrt{\text{Hz}}$. Such a NET aligns with the sensitivities of advanced solid-state thermometers [41] and qualifies the TMA as a promising preamplification stage for bolometers.

C. Fully photonic design

The blueprint we provided above allows for numerous developments. One of the most promising possibilities is a device in which photons constitute all heat transport channels between the terminals. This design variation is illustrated in Fig. 6. Such a device can operate thanks to the possibility of having heavily doped, locally metallic regions within the Anderson insulators, as described in Sec. II. Suppose we connect a metallic reservoir, such

as the gate or the drain, to a single, continuous metallic region in the central island through lossless lines. In that case, we create a photonic heat transport channel between two Ohmic impedances whose transmission coefficient is nearly unaffected by temperature variations. This differs from the source-island connection because, in that scenario, the Ohmic regions in contact with the lines are separated and in series with the Anderson insulator.

The degree of freedom provided by the choice of R_g and R_d is replaced by the matching of the impedances of the Ohmic regions and the corresponding terminals, which impacts the τ of the specific channel as per Eq. 1. Notably this proposal follows the same scaling in temperatures for all the heat channels as the previously proposed devices so we can expect very similar performances. A fully photonic PHA can connect reservoirs over great distances, utilizing the advantages of photon-mediated heat transport [12] while offering a flexible design that allows tunable elements to control the transmission. This geometry in principle has a limited flow of heat (quantum heat conductance) in the photonic channel but this is essentially shared with the previous proposal where in any case the source heat channel was photonic. Furthermore, capacitors can be eventually integrated into the lines, providing a full non-galvanic coupling to the terminals.

V. CONCLUSIONS

This paper proposes a device that achieves NDTC using electromagnetic fluctuations for heat exchange. While it has been observed and utilized in a heat amplifier based on near-field radiation [42], a mesoscale integrated solid-state demonstration of NDTC and heat amplification is still lacking. Our proposal is a possible answer to this gap. Depending on the configuration, the PHA can function either as a heat current modulation or a temperature modulation amplifier. We demonstrate that this device can achieve amplification factors up to 15 in the former regime and 2.5 in the latter. The device exhibits low relaxation times, indicating that its operational speed aligns with other experimentally tested microscopic thermal devices [36].

The PHA may represent one of the essential components for executing a fully thermal logic, as previously suggested within phononic [43] and phase-coherent electronic [44] heat transport frameworks, with electromagnetic fluctuations propagating in waveguides. Relying on these fluctuations means also being compatible with the established framework of circuit quantum electrodynamics [45] and thermodynamics [46]. This architecture can manage and harvest the waste heat from other devices or the attenuation stages of electrical lines [38] to power other processes. Complete control of spurious heat can be helpful to power operations that have already been demonstrated, such as refrigerators compatible with photon-mediated heat transport [47, 48].

The PHA's performance as a thermal transistor, en-

abling control of the source-drain current by the gate temperature, can also be exploited for automatic on-chip heat regulation. For example, the device could switch to the “ON” state when the gate temperature crosses a certain threshold and cool the source terminal by letting a significant amount of heat flow out of it.

Furthermore, in its temperature modulation amplifier configuration, the PHA presents an intriguing possibility for sensing and monitoring device temperatures, serving as an amplification stage for on-chip thermometers. For instance, in the case of bolometers, such amplification enables the detection of more minor temperature fluctuations without diminishing the heat capacity of the absorber, thereby enhancing its sensitivity.

Compared to other mesoscopic devices, our proposal is based on photonic transport along lossless lines, which operates efficiently at the cryogenic temperatures needed for specific implementations of quantum technologies and can also be integrated into solid-state setups. Our design can be adapted to either harness electron- and photon-mediated heat transport or entirely rely on the latter, as discussed in Sec. IV C.

Studies have shown that heat transport along superconducting lines remains effective over long distances and can be controlled by incorporating tunable impedances [12–14, 49]. Utilizing photons as heat carriers also offers the advantage of avoiding galvanic coupling to the target devices [50], a feature that could be beneficial when high coherence is essential, such as in qubit thermal management [51, 52]. Another potential direction is integrating multiple parallel lossless lines into the design to enhance conductivity between the source and the central island, thus improving power performance.

Other applications of this design can leverage its bistability, achievable through careful selection of parameters, especially the Anderson temperature T_a . The two possible equilibrium states in this configuration can function eventually as the states of a register [53].

ACKNOWLEDGMENTS

We acknowledge the EU’s Horizon 2020 Research and Innovation Framework Programme under Grants No. 964398 (SUPERGATE), No. 101057977 (SPECTRUM), and the PNR MUR project PE000023-NQSTI for partial financial support. A.B. acknowledges the MUR-PRIN2022 Project NETHQS (Grant No. 2022B9P8LN) and CNR project QTHERMONANO.

Appendix A: Thermal conductances

The expressions of the thermal conductances of the colder Anderson insulator with respect to all the other reservoirs employed in the main text are obtained by deriving the formulae of the thermal currents by T_1 for the

different heat transport channels. We also correctly considered the current conventions adopted in the main text (see Sec. II).

The κ_γ , fundamental in the functioning of the PHA, is already discussed in the main text in Eq. 5 due to its relevance. The heat conductances of the tunnel contacts with the gate and the drain, respectively κ_g and κ_d , are obtained by deriving Eq. 6:

$$\kappa_{g,d} = \left| \frac{\partial J_{g,d}}{\partial T_1} \right| = \frac{\pi^2 k_B^2}{3e^2 R_{g,d}} T_1. \quad (\text{A1})$$

We took the absolute value because we want to compute the differential flow of heat outside of the colder Anderson insulator, given the adopted heat current convention. Instead, the heat conductance lost in the phononic degrees of freedom is:

$$\kappa_{ph} = \frac{\partial J_{ph}}{\partial T_1} = 6\Sigma VT_1^5, \quad (\text{A2})$$

simply obtained by the derivative of Eq. 7. The phononic contribution decreases faster than all the other conductances at low temperatures, becoming less important with reducing temperatures.

Appendix B: SFDR estimate

The *SFDR* is computed, as told in Secs. IV A - IV B, from the coefficients of the Fourier series of the responses to a sinusoidal input. In particular, for the CMA, the expression of the input is the following:

$$J_{g,in,CMA}(T_{g0}, \Delta J_g; t) = J_{g0}(T_{g0}) + \Delta J_g \sin(t) \quad (\text{B1})$$

where J_{g0} is the gate current in the system when $T_g = T_{g0}$.

Instead, the TMA input is written as:

$$T_{g,in,TMA}(T_{g0}, \Delta T_g; t) = T_{g0} + \Delta T_g \sin(t). \quad (\text{B2})$$

Then, the respective outputs, $J_d(t)$ for the CMA and $T_1(t)$ for the TMA, can be evaluated by numerically solving Eq. 8 for T_1 and, in the case of $J_d(t)$, substituting the result back into the expression of the drain current. The numerically computed Fourier series coefficients of these outputs A_i , where i is the multiple of the input frequency, are employed for calculating the *SFDR* according to the methodology discussed in Eq. 14.

Appendix C: Noise estimate

We calculated the low-frequency power fluctuations spectral densities from the tunnel contacts and the phonon bath to the central island by following Refs. [54] and [34]. The expression is computed by using the fact

that a tunnel junction follows Poissonian statistics, so noise density is given ($i = g, d$) by:

$$\mathcal{N}_i^2 = \frac{2}{e^2 R_i} \int_{-\infty}^{+\infty} \epsilon^2 [f(\epsilon, T_i) + f(\epsilon, T_1) - 2f(\epsilon, T_i)f(\epsilon, T_1)] d\epsilon, \quad (\text{C1})$$

where $f(\epsilon, T)$ is the Fermi distribution at energy ϵ and temperature T . It is important to note that due to the tunneling nature of the problem, the same general formula applies to the case of terminals with strong (non-linear) temperature differences.

Instead, the spectral thermal noise density due to the

$$\mathcal{N}_\gamma^2 = \frac{\tau}{4\pi\hbar} \int_{-\infty}^{+\infty} \epsilon^2 \left[\coth\left(\frac{\epsilon}{2k_B T_s}\right) \coth\left(\frac{\epsilon}{2k_B T_1}\right) - 1 \right] d\epsilon, \quad (\text{C3})$$

where τ is taken outside of the integral being frequency (energy) independent. Note that all these expressions, for identical temperatures T , correspond to the thermal noise limit $\mathcal{N}_i^2 = 4k_B \kappa_i T^2$, where the subscript $i = \gamma, g, d, ph$ identifies the heat transport channel of conductance κ_i [9].

The noise estimate of Sec. IV A is obtained from the components of the power fluctuations on the central island presented above, evaluated for the CMA device. The results are given for a gate temperature of 260 mK, for which the device achieves the maximum amplification factor of around 20 for both the drain and the source outputs. We obtained, respectively, for the gate, the drain, the phonon bath, and the source contributions the following values:

$$\mathcal{N}_{g,CMA}^2 \approx 1.9 \times 10^{-12} \text{ (pW)}^2/\text{Hz}, \quad (\text{C4})$$

$$\mathcal{N}_{d,CMA}^2 \approx 7.9 \times 10^{-13} \text{ (pW)}^2/\text{Hz}, \quad (\text{C5})$$

$$\mathcal{N}_{ph,CMA}^2 \approx 2.1 \times 10^{-13} \text{ (pW)}^2/\text{Hz}, \quad (\text{C6})$$

$$\mathcal{N}_{\gamma,CMA}^2 \approx 1.2 \times 10^{-12} \text{ (pW)}^2/\text{Hz}. \quad (\text{C7})$$

These values, assumed to be uncorrelated, sum up to a total of a fluctuation spectral density on the output of $\mathcal{N}_{CMA,out}^2 \approx 4.1 \times 10^{-12} \text{ (pW)}^2/\text{Hz}$. Considering an amplification factor of 20, the Noise Equivalent Power on the input results to be

$$\text{NEP}_{CMA} = \sqrt{\mathcal{N}_{CMA,out}^2}/20 \approx 1.0 \times 10^{-7} \text{ pW}/\sqrt{\text{Hz}}.$$

thermal contact with the phonon bath is [34]:

$$\mathcal{N}_{ph}^2 = 12k_B V \Sigma (T_b^7 + T_1^7), \quad (\text{C2})$$

where we have considered the appropriate power laws of the electron-phonon coupling of the considered Anderson insulators [28].

The investigation of the noise and fluctuation in systems with substantial temperature differences has been discussed deeply only recently [55–60]. However, for the power fluctuations of the photonic channel, we refer to the framework recently presented in Ref. [61] adapted to our device's frequency-independent model of two purely dissipative impedances (pure resistances). Indeed, for tiny fluctuations, we got an expression for the spectral density of the fluctuations on the central island due to the source terminal heat inflow

In the same way, it is possible to evaluate the low-frequency fluctuation spectral density contributions from the various components in the TMA device (Sec. IV B). In particular, estimating the noise equivalent temperature fluctuation at the TMA input (gate) is possible. In this case, we evaluate the four contributions for the configuration of maximum gain at $T_g = 310$ mK we get

$$\mathcal{N}_{g,TMA}^2 \approx 1.7 \times 10^{-12} \text{ (pW)}^2/\text{Hz}, \quad (\text{C8})$$

$$\mathcal{N}_{d,TMA}^2 \approx 1.5 \times 10^{-12} \text{ (pW)}^2/\text{Hz}, \quad (\text{C9})$$

$$\mathcal{N}_{ph,TMA}^2 \approx 9.5 \times 10^{-13} \text{ (pW)}^2/\text{Hz}, \quad (\text{C10})$$

$$\mathcal{N}_{\gamma,TMA}^2 \approx 2.4 \times 10^{-12} \text{ (pW)}^2/\text{Hz}. \quad (\text{C11})$$

We then take the square root of their sum (since we again assume independent fluctuations) and convert it to the output T_1 temperature oscillations by dividing by the total thermal differential conductance [62] $\kappa_{tot} = 0.16 \text{ pW/K}$ (evaluated as the sum of the conductance formulas presented in Appendix A) so that we get the amplitude of the corresponding temperature oscillations on the output [41], which we can then be divided by the gain of $\mathcal{G} = 2.5$ to obtain the input equivalent spectral density

$$\text{NET}_{TMA} \approx 5.6 \text{ }\mu\text{K}/\sqrt{\text{Hz}}, \quad (\text{C12})$$

which is compatible with the expected noise performances of the most advanced low-temperature solid-state thermometers [41].

[1] A. Fornieri and F. Giazotto, Towards phase-coherent caloritronics in superconducting circuits, Nat. Nanotech-

- [2] T. Swoboda, K. Klinar, A. S. Yalamarthy, A. Kitanovski, and M. M. Rojo, Solid-state thermal control devices, *Adv. Electron. Mater.* **7**, 2000625 (2021).
- [3] L. Castelli, Q. Zhu, T. J. Shimokusu, and G. Wehmeyer, A three-terminal magnetic thermal transistor, *Nat. Commun.* **14**, 393 (2023).
- [4] X. Siqi, Z. Hongxin, Z. Xing, and W. Haidong, A brief review on the recent development of phonon engineering and manipulation at nanoscales, *Int. J. Extreme Manuf.* **6**, 012007 (2023).
- [5] O.-P. Saira, M. Meschke, F. Giazotto, A. M. Savin, M. Möttönen, and J. P. Pekola, Heat transistor: Demonstration of gate-controlled electronic refrigeration, *Phys. Rev. Lett.* **99**, 027203 (2007).
- [6] S. Krinner, S. Storz, P. Kurpiers, P. Magnard, J. Heinsoo, R. Keller, J. Lütolf, C. Eichler, and A. Wallraff, Engineering cryogenic setups for 100-qubit scale superconducting circuit systems, *EPJ Quantum Technol.* **6**, 2 (2019).
- [7] A. Somoroff, Q. Ficheux, R. A. Mencia, H. Xiong, R. Kuzmin, and V. E. Manucharyan, Millisecond coherence in a superconducting qubit, *Phys. Rev. Lett.* **130**, 267001 (2023).
- [8] A. Romanenko, R. Pilipenko, S. Zorzetti, D. Frolov, M. Awida, S. Belomestnykh, S. Posen, and A. Grassellino, Three-dimensional superconducting resonators at 20 mK with photon lifetimes up to $\tau = 2$ s, *Phys. Rev. Appl.* **13**, 034032 (2020).
- [9] F. Giazotto, T. T. Heikkilä, A. Luukanen, A. M. Savin, and J. P. Pekola, Opportunities for mesoscopics in thermometry and refrigeration: Physics and applications, *Rev. Mod. Phys.* **78**, 217 (2006).
- [10] M. Meschke, W. Guichard, and J. P. Pekola, Single-mode heat conduction by photons, *Nature* **444**, 187 (2006).
- [11] T. Ojanen and A.-P. Jauho, Mesoscopic photon heat transistor, *Phys. Rev. Lett.* **100**, 155902 (2008).
- [12] M. Partanen, K. Y. Tan, J. Govenius, R. E. Lake, M. K. Mäkelä, T. Tantt, and M. Möttönen, Quantum-limited heat conduction over macroscopic distances, *Nat. Phys.* **12**, 460 (2016).
- [13] A. Ronzani, B. Karimi, J. Senior, Y.-C. Chang, J. T. Peltonen, C. Chen, and J. P. Pekola, Tunable photonic heat transport in a quantum heat valve, *Nat. Phys.* **14**, 991 (2018).
- [14] D. Subero, O. Maillet, D. S. Golubev, G. Thomas, J. T. Peltonen, B. Karimi, M. Marín-Suárez, A. L. Yeyati, R. Sánchez, S. Park, and J. P. Pekola, Bolometric detection of Josephson inductance in a highly resistive environment, *Nat. Commun.* **14**, 7924 (2023).
- [15] A. Iorio, E. Strambini, G. Haack, M. Campisi, and F. Giazotto, Photonic heat rectification in a system of coupled qubits, *Phys. Rev. Appl.* **15**, 054050 (2021).
- [16] J. P. Pekola and B. Karimi, Colloquium: Quantum heat transport in condensed matter systems, *Rev. Mod. Phys.* **93**, 041001 (2021).
- [17] G. Marchegiani, A. Braggio, and F. Giazotto, Highly efficient phase-tunable photonic thermal diode, *Appl. Phys. Lett.* **118**, 022602 (2021).
- [18] J. Senior, A. Gubaydullin, B. Karimi, J. T. Peltonen, J. Ankerhold, and J. P. Pekola, Heat rectification via a superconducting artificial atom, *Commun. Phys.* **3**, 40 (2020).
- [19] A. Gubaydullin, G. Thomas, D. S. Golubev, D. Lvov, J. T. Peltonen, and J. P. Pekola, Photonic heat transport in three terminal superconducting circuit, *Nat. Commun.* **13**, 1552 (2022).
- [20] B. Li, L. Wang, and G. Casati, Negative differential thermal resistance and thermal transistor, *Appl. Phys. Lett.* **88**, 143501 (2006).
- [21] J.-H. Jiang, M. Kulkarni, D. Segal, and Y. Imry, Phonon thermoelectric transistors and rectifiers, *Phys. Rev. B* **92**, 045309 (2015).
- [22] W. Rongqian, W. Chen, L. Jincheng, and J. Jian-Hua, Inelastic thermoelectric transport and fluctuations in mesoscopic systems, *Adv. Phys.: X* **7**, 2082317 (2022).
- [23] L. M. A. Pascal, H. Courtois, and F. W. J. Hekking, Circuit approach to photonic heat transport, *Phys. Rev. B* **83**, 125113 (2011).
- [24] M. Majland, K. S. Christensen, and N. T. Zinner, Quantum thermal transistor in superconducting circuits, *Phys. Rev. B* **101**, 184510 (2020).
- [25] D. R. Schmidt, R. J. Schoelkopf, and A. N. Cleland, Photon-mediated thermal relaxation of electrons in nanostructures, *Phys. Rev. Lett.* **93**, 045901 (2004).
- [26] S. S. Dey, G. Timossi, L. Amico, and G. Marchegiani, Negative differential thermal conductance by photonic transport in electronic circuits, *Phys. Rev. B* **107**, 134510 (2023).
- [27] A. L. Efros and B. I. Shklovskii, Coulomb gap and low temperature conductivity of disordered systems, *J. Phys. C* **8**, L49 (1975).
- [28] N. Wang, F. Wellstood, B. Sadoulet, E. E. Haller, and J. Beeman, Electrical and thermal properties of neutron-transmutation-doped Ge at 20 mK, *Phys. Rev. B* **41**, 3761 (1990).
- [29] E. E. Haller, K. M. Itoh, and J. W. Beeman, Neutron transmutation doped (NTD) germanium thermistors for sub-mm bolometer applications, in *Submillimetre and Far-Infrared Space Instrumentation, Proceedings of the 30th ESLAB Symposium held in Noordwijk, 24-26 September 1996*, edited by E. Rolfe and G. Pilbratt (European Space Agency, Paris, 1996) p. 115.
- [30] D. McCammon, Semiconductor thermistors, in *Cryogenic Particle Detection* (Springer Berlin Heidelberg, Berlin, Heidelberg, 2005).
- [31] A. Fornieri, G. Timossi, R. Bosisio, P. Solinas, and F. Giazotto, Negative differential thermal conductance and heat amplification in superconducting hybrid devices, *Phys. Rev. B* **93**, 134508 (2016).
- [32] F. Giazotto, T. T. Heikkilä, A. Luukanen, A. M. Savin, and J. P. Pekola, Opportunities for mesoscopics in thermometry and refrigeration: Physics and applications, *Rev. Mod. Phys.* **78**, 217 (2006).
- [33] E. Olivieri, M. Barucci, J. Beeman, L. Risegari, and G. Ventura, Excess heat capacity in NTD Ge thermistors, *J. Low Temp. Phys.* **143**, 153 (2006).
- [34] F. Vischi, M. Carrega, A. Braggio, F. Paolucci, F. Bianco, S. Roddaro, and F. Giazotto, Electron cooling with graphene-insulator-superconductor tunnel junctions for applications in fast bolometry, *Phys. Rev. Appl.* **13**, 054006 (2020).
- [35] D. L'Hôte, X. F. Navick, R. Tourbot, J. Mangin, and F. Pesty, Charge and heat collection in a 70 g heat/ionization cryogenic detector for dark matter search, *J. Appl. Phys.* **87**, 1507 (2000).
- [36] L. Man, W. Huan, M. A. Erin, Q. Zihao, P. G. Dominic, D. N. Huu, L. Tianhan, S. W. Paul, and H. Yongjie, Electrically gated molecular thermal switch, *Science* **382**,

- 585 (2023).
- [37] F. Paolucci, G. Marchegiani, E. Strambini, and F. Giazotto, Phase-tunable temperature amplifier, *Europhys. Lett.* **118**, 68004 (2017).
- [38] Y. Li, Y. Dang, S. Zhang, X. Li, Y. Jin, P. Ben-Abdallah, J. Xu, and Y. Ma, Radiative thermal transistor, *Phys. Rev. Appl.* **20**, 024061 (2023).
- [39] G. D. Simoni and F. Giazotto, Ultralinear magnetic-flux-to-voltage conversion in superconducting quantum interference proximity transistors, *Phys. Rev. Appl.* **19**, 054021 (2023).
- [40] A. L. Efros and B. I. Shklovskii, *Electronic Properties of Doped Semiconductors* (Springer-Verlag, Heidelberg, 1984).
- [41] S. Gasparinetti, K. L. Viisanen, O.-P. Saira, T. Faivre, M. Arzeo, M. Meschke, and J. P. Pekola, Fast electron thermometry for ultrasensitive calorimetric detection, *Phys. Rev. Appl.* **3**, 014007 (2015).
- [42] P. Ben-Abdallah and S.-A. Biehs, Near-field thermal transistor, *Phys. Rev. Lett.* **112**, 044301 (2014).
- [43] L. Wang and B. Li, Thermal logic gates: Computation with phonons, *Phys. Rev. Lett.* **99**, 177208 (2007).
- [44] F. Paolucci, G. Marchegiani, E. Strambini, and F. Giazotto, Phase-tunable thermal logic: Computation with heat, *Phys. Rev. Appl.* **10**, 024003 (2018).
- [45] A. Blais, A. L. Grimsmo, S. M. Girvin, and A. Wallraff, Circuit quantum electrodynamics, *Rev. Mod. Phys.* **93**, 025005 (2021).
- [46] J. P. Pekola, Towards quantum thermodynamics in electronic circuits, *Nat. Phys.* **11**, 118 (2015).
- [47] M. A. Aamir, P. Jamet Suria, J. Marín Guzmán, C. Castillo-Moreno, J. M. Epstein, N. Yunger Halpern, and S. Gasparinetti, Thermally driven quantum refrigerator autonomously resets a superconducting qubit, *Nat. Phys.* 10.1038/s41567-024-02708-5 (2025).
- [48] H. Kivijärvi, A. Viitanen, T. Mörstedt, and M. Möttönen, Noise-induced quantum-circuit refrigeration, arXiv:2412.05886.
- [49] O. Maillet, D. Subero, J. T. Peltonen, D. S. Golubev, and J. P. Pekola, Electric field control of radiative heat transfer in a superconducting circuit, *Nat. Commun.* **11**, 4326 (2020).
- [50] F. Paolucci, G. Timossi, P. Solinas, and F. Giazotto, Coherent manipulation of thermal transport by tunable electron-photon and electron-phonon interaction, *J. Appl. Phys.* **121**, 244305 (2017).
- [51] T. Yoshioka, H. Mukai, A. Tomonaga, S. Takada, Y. Okazaki, N.-H. Kaneko, S. Nakamura, and J.-S. Tsai, Active initialization experiment of a superconducting qubit using a quantum circuit refrigerator, *Phys. Rev. Appl.* **20**, 044077 (2023).
- [52] S. Nakamura, T. Yoshioka, S. Lemziakov, D. Lvov, H. Mukai, A. Tomonaga, S. Takada, Y. Okazaki, N.-H. Kaneko, J. Pekola, and J.-S. Tsai, Probing fast quantum circuit refrigeration in the quantum regime, *Phys. Rev. Appl.* **23**, L011003 (2025).
- [53] V. Kubyskyi, S.-A. Biehs, and P. Ben-Abdallah, Radiative bistability and thermal memory, *Phys. Rev. Lett.* **113**, 074301 (2014).
- [54] D. Golubev and L. Kuzmin, Nonequilibrium theory of a hot-electron bolometer with normal metal-insulator-superconductor tunnel junction, *J. Appl. Phys.* **89**, 6464 (2001).
- [55] D. S. Golubev and J. P. Pekola, Statistics of heat exchange between two resistors, *Phys. Rev. B* **92**, 085412 (2015).
- [56] O. S. Lumbroso, L. Simine, A. Nitzan, D. Segal, and O. Tal, Electronic noise due to temperature differences in atomic-scale junctions, *Nature* **562**, 240 (2018).
- [57] E. Sivrie, H. Duprez, A. Anthore, A. Aassime, F. D. Parmentier, A. Cavanna, A. Ouerghi, U. Gennser, and F. Pierre, Electronic heat flow and thermal shot noise in quantum circuits, *Nat. Commun.* **10**, 5638 (2019).
- [58] S. Larocque, E. Pinsolle, C. Lupien, and B. Reulet, Shot noise of a temperature-biased tunnel junction, *Phys. Rev. Lett.* **125**, 106801 (2020).
- [59] L. Tesser, M. Acciai, C. Spånslätt, J. Monsel, and J. Splettstoesser, Charge, spin, and heat shot noises in the absence of average currents: Conditions on bounds at zero and finite frequencies, *Phys. Rev. B* **107**, 075409 (2023).
- [60] L. Pierattelli, F. Taddei, and A. Braggio, ΔT -noise in multiterminal hybrid systems, arXiv:2411.12572.
- [61] M. Hübner, D. M. Basko, and W. Belzig, Scattering approach to near-field radiative heat transfer, arXiv:2411.04048.
- [62] P. L. Richards, Bolometers for infrared and millimeter waves, *J. Appl. Phys.* **76**, 1 (1994).